

RXTE Observations of the Low-Mass X-Ray Binary 4U 1608–522 in Upper-Banana State

Hiromitsu Takahashi

*Hiroshima Astrophysical Science Center, Hiroshima University, 1-3-1 Kagamiyama,
Higashi-Hiroshima, Hiroshima 739-8526, Japan*

hirotaka@hep01.hepl.hiroshima-u.ac.jp

and

Soki Sakurai and Kazuo Makishima

*Department of Physics, University of Tokyo, 7-3-1 Hongo, Bunkyo-ku, Tokyo 113-0033,
Japan*

ABSTRACT

To investigate the physics of mass accretion onto weakly-magnetized neutron stars, 95 archival *RXTE* data sets of an atoll source 4U 1608–522, acquired over 1996–2004 in so-called upper-banana state, were analyzed. The object meantime exhibited 3–30 keV luminosity in the range of $\lesssim 10^{35} - 4 \times 10^{37}$ erg s $^{-1}$, assuming a distance of 3.6 kpc. The 3–30 keV PCA spectra, produced one from each dataset, were represented successfully with a combination of a soft and a hard component, of which the presence was revealed in a model-independent manner by studying spectral variations among the observations. The soft component is expressed by so-called multi-color disk model with a temperature of ~ 1.8 keV, and is attributed to the emission from an optically-thick standard accretion disk. The hard component is a blackbody emission with a temperature of ~ 2.7 keV, thought to be emitted from the neutron-star surface. As the total luminosity increases, a continuous decrease was observed in the ratio of the blackbody luminosity to that of the disk component. This property suggests that the matter flowing through the accretion disk gradually becomes difficult to reach the neutron-star surface, presumably forming outflows driven by the increased radiation pressure. On time scales of hours to days, the overall source variability was found to be controlled by two independent variables; the mass accretion rate, and the innermost disk radius which changes both physically and artificially.

Subject headings: stars: binaries: general — stars: individual(4U 1608–522) — stars: neutron — X-ray: stars

1. INTRODUCTION

It has long been known that low-mass X-ray binaries (LMXBs), namely close binaries involving neutron stars (NSs) without strong magnetic fields, emit thermal type spectra when they are luminous ($\gtrsim 10^{36}$ erg s $^{-1}$). In the 1970’s, their spectra were often modeled empirically in terms of simple thermal Bremsstrahlung, without much physical basis. As observations made progress, it gradually became clear that this simple empirical modeling is in fact inadequate, and at least two components are needed to describe wide-band (typically 2–30 keV) LMXB spectra. Today, a canonical model (sometimes called “Eastern model”) interprets the X-ray spectra of a luminous LMXB as originating from two major emission regions; the surface of the NS (or often called “boundary layer”) and an accretion disk around it (Mitsuda et al. 1984).

The Eastern model was constructed based on *Tenma* observations of luminous LMXBs (Mitsuda et al. 1984, 1989; Makishima et al. 1989), particularly considering intensity-correlated spectral changes. When an LMXB becomes brighter on a time scale of ~ 1000 s, its spectrum hardens in energies from ~ 2 to ~ 10 keV, but the spectral shape in the hardest range (above 10 keV) stays constant. A difference between a pair of spectra with different intensities generally takes a form of a blackbody (BB) spectrum, of which the intensity changes but the shape (i.e., the temperature) is approximately constant. This BB component has a temperature of ~ 2 keV, which is close to the Eddington temperature, 2.0 keV, for a NS of $\sim 1.4 M_{\odot}$ mass (with M_{\odot} being the solar mass) and 10 km radius. In addition, the area of its emission region is inferred to be a fraction of the surface area of such a NS. Therefore, the BB component has been ascribed successfully to the NS surface emission. Indeed, every spectrum observed from these sources was reproduced by a sum of this BB component, and an additional soft component. The soft component was approximated first by a softer BB of ~ 1 keV temperature, but later, much better by a particular superposition of BB spectra, called “disk blackbody” or “multi-color disk” (MCD) emission (Mitsuda et al. 1984; Makishima et al. 1989), as predicted by the optically-thick standard accretion disk model (Shakura & Sunyaev 1973).

While the Eastern model thus provides a promising ground to understand the physics of mass accretion in luminous LMXBs, their complex spectral and intensity variations have often been described in a purely empirical manner using “color-color” diagrams and other similar methods. As a result, such empirical classifications as “Z sources” and “atoll sources” have been created, together with various “branches” on these empirical diagrams (e.g., Hasinger & van der Klis 1989). These primitive descriptions are waiting to be replaced by more physically meaningful ones, using the Eastern model.

After the launch in 1995, the *Rossi X-Ray Timing Explorer* (*RXTE*; Bradt et al. 1993)

has been observing many LMXBs for a huge number of times. With the largest effective area and the highest timing resolution ever achieved, *RXTE* is indeed very suitable to the study of spectral variations of LMXBs. On time scales of milliseconds to seconds, Gilfanov et al. (2003) and Revnivtsev & Gilfanov (2006) carried out such studies using the *RXTE* data, and revealed that the variation is carried by a rather hard BB-like emission component with a temperature of $\sim 2\text{--}3$ keV. These results reinforce the validity of the Eastern model, and encourage us to attempt its extensive application to the *RXTE* data of LMXBs. We thus hope to understand the spectral variations of LMXBs as a whole using a physical model (based on the Eastern description).

As the first of a series of our planned publications, the present paper deals with so-called upper-banana state of 4U 1608–522, which is one of the most frequently observed atoll sources by *RXTE*. Section 2 describes 414 *RXTE* data sets of this LMXB, of which 95 are selected for use in the present paper. In § 3.1, we select four representative spectra out of the 95 data sets, and analyze their intensity-correlated spectral changes to reconstruct the Eastern model. The derived model parameter values are examined in § 3.2, followed by § 3.3 where the model is applied to all the 95 energy spectra and relations among the obtained physical parameters are studied. As a reconfirmation of our approach, we calculate in § 3.4 the effective degrees of freedom involved in the variability, of which the results are physically interpreted in § 3.5. As discussed in § 4, the results give a full support to the Eastern model, and lead to a finding of mass outflows as the source gets luminous.

2. OBSERVATIONS AND DATA REDUCTION

Our target object 4U 1608–522 is an LMXB with a recurrent transient characteristic, exhibiting occasional outbursts. As the X-ray intensity evolves through these outbursts, the source is known to take all three spectral states of atoll sources (Hasinger & van der Klis 1989); namely island, lower-banana, and upper-banana states, in the increasing order of the source intensity (Muno et al. 2002; Gierliński & Done 2002a). In the island and lower-banana states, a hard tail appears in the spectra presumably due to Comptonization by hot electrons, of which the temperature is of the order of several tens keV (Gierliński & Done 2002b). In the present paper, we analyze only the data in the upper-banana state, where the spectrum takes the thermal-shape characteristic of luminous LMXBs. The original paper by Mitsuda et al. (1984) also utilized 4U 1608–522, when the source was presumably in the upper-banana state. The source distance is assumed to be 3.6 kpc (Nakamura et al. 1989).

Although *RXTE* has observed many outbursts from 4U 1608–522, we limit the present study to those data sets which were obtained from the launch of *RXTE* (December 1995)

to the end of August 2004, when the brightest and the second brightest outbursts were recorded. During the period, 414 pointing observations of 4U 1608–522 were conducted with the Proportional Counter Array (PCA; Jahoda et al. 1996). Although some of the five Proportional Counter Units (PCUs) of the PCA were turned off in some observations, PCU2 alone was always operational. In order to avoid systematic differences among different PCUs, we utilized the PCU2 data only, because the source in the upper-banana state is very bright (typically ~ 1000 counts s^{-1} per PCU) and hence statistical errors are usually negligible. We employed “Standard-2” data, of which the time resolution is 16 s, since they are most accurately calibrated and suitable for spectral analysis. The data were filtered in the standard manner for bright sources, and were corrected for dead times in the standard way. The PCA background was estimated for each dataset by PCABACKEST version 3.0. To remove Type I bursts, we excluded those time regions when the background-subtracted source count rates (per 16 s) are outside 50%–200% of the average over each observation.

After the subtraction of the modeled background, we calculated color-color diagrams (CCDs) and hardness-intensity diagrams (HIDs) of 4U 1608–522 using data points averaged over 128 s. In this paper, the soft and hard colors refer to 6–10 keV vs. 2.5–6 keV source count ratios and those in 10–30 keV vs. 6–10 keV, respectively. The intensity used for HIDs refers to an energy band of 2.5–30 keV in the unit of the Crab Nebula count rate. As described in Jahoda et al. (2006), the overall PCA operation history is divided into 5 epochs according to differences in the high-voltage settings. As a result, CCDs and HIDs need to be produced separately for different epochs. Figure 1 representatively shows the obtained CCD and HIDs of 72 observations in the entire epoch 3. Here, we excluded faint data points of which the intensities are less than $10 \text{ counts s}^{-1} \text{ PCU2}^{-1}$ ($\lesssim 3 \times 10^{35} \text{ erg s}^{-1}$ for 3.6 kpc).

On the CCD of Figure 1, the count rate increases from top through lower left to lower right, with each part corresponding to the island, lower-banana, and upper-banana states, respectively. On the HIDs, the data points form many vertical line-like features, or stripes. The source traces these stripes on a time scale of days, and moves horizontally on much longer time scales. The former causes the source motion within a single state on the CCD, while the latter leads to transitions among the three states. The hard color is higher in the island state, and decreases in the banana states. The present paper focuses on the upper-banana state, which is defined here as those datasets with the 3–30 keV source intensity exceeding 0.4 Crab. We applied the same criteria to the data from the other four epochs. When summed over the 5 epochs, the selected datasets reach 95 in number, with their 3–30 keV luminosities spanning a range of $(1\text{--}4) \times 10^{37} \text{ erg s}^{-1}$. Some of these datasets were already analyzed with the Eastern model by Gierliński & Done (2002b), Gilfanov et al. (2003) and Lin et al. (2007).

For each dataset in the upper-banana state, we accumulated the Standard-2 data into a single 3–30 keV spectrum, with a typical exposure of several ks. Then, the modeled background mentioned above was subtracted. However, this method is known to causes slight (several percents) over-subtraction of the background ¹. This effect was compensated for by rescaling the background spectrum up to 10%, so that its count rate matches that of the on-source data in the hardest 60–100 keV energy range, where the signal count is considered negligible. Since the source count was detected significantly up to 30 keV, we hereafter analyze the total 95 energy spectra in the energy range of 3–30 keV. The PCU2 response matrix was created for each observation using PCARSP version 10.1. In order to take into account calibration uncertainties, we add 1% and 7% systematic errors to each energy bin of the source and background spectra, respectively.

3. DATA ANALYSIS AND RESULTS

3.1. Comparison of Energy Spectra

In comparison with the previous work by Mitsuda et al. (1984), we first examine relatively slow ($\gtrsim 10^3$ s) spectral variations along the upper-banana state of 4U 1608–522. For this purpose, we selected four representative spectra, hereafter Spec A through Spec D, obtained at the most luminous (several times 10^{37} erg s^{−1}) end (i.e., the right side) of the HIDs. Three of them (Spec A, Spec B and Spec C) come from the same vertical line, while the other is located on the different line. Their observation IDs, average intensities, and soft/hard colors are summarized in Table 1, while their locations on the hard-HID are indicated in Figure 1. These spectra and their ratios to their average spectrum are shown in Figure 2.

In Figure 2, the brightest (Spec A) and the second brightest (Spec B) spectra of the four are selected from the same vertical line in the HID. By comparing them, it is clear that the intensity in the hard energy band changes significantly, while that in the soft band is kept constant. Moreover, in energies above ~ 15 keV, their ratios saturates as a function of energy. As originally proposed by Mitsuda et al. (1984), these results can be explained when the spectra consist of a variable hard component that dominates in $\gtrsim 15$ keV energy band and a stable soft component, and the normalization (but not the shape) of the former changes between the two spectra. Indeed, the difference spectrum between them, shown in Figure 3 as Spec 1, is represented successfully by a BB model of which the temperature is

¹<http://lheawww.gsfc.nasa.gov/users/craigm/pca-bkg-tdrift/>

$kT_{\text{BB}} \sim 2.5$ keV. The obtained best-fit parameters are summarized in Table 2. Although the derived absorption column density, $\sim 3 \times 10^{23} \text{ cm}^{-2}$, is significantly higher than that reported previously ($0.8 \times 10^{22} \text{ cm}^{-2}$; Grindlay & Liller 1978; Rutledge et al. 1999), the difference may be attributed to slight changes in the assumed stable soft component (as assessed later in this subsection), and/or those in kT_{BB} . These results reconfirm the achievements with *Tenma* (Mitsuda et al. 1984) and *Ginga* (Makishima et al. 1989).

From the above results, we consider that the harder part of the spectrum is carried by a “hard component” which is approximated by a $kT_{\text{BB}} \sim 2.5$ keV BB. Its variation (in normalization rather than in kT_{BB} ; Makishima et al. 1989) causes significant changes in the hard color, but does not affect the intensity very much because the total source counts are dominated by softer photons. This explains the formation of the vertical stripes in the hard HID of Figure 1. This hard component is most naturally attributed to optically-thick emission from the NS surface, because the measured temperature agrees with the local Eddington temperature of a $1.4 M_{\odot}$ NS, or ~ 2.0 keV.

Contrary to the above case, the other two spectra, the faintest spectrum (Spec D) and the second faintest one (Spec C) which lie on a pair of stripes adjacent to each other, differ mainly in the soft energy band, with the hard energy end kept almost constant. This suggests that the source variation in this case is carried by a soft spectral component which is presumably identified as the stable component suggested by Spec A and Spec B. To constrain its spectral shape, we derived the difference spectrum (denoted Spec 2) between Spec C and Spec D, and show the results in Figure 4. Clearly, this difference spectrum is much softer than the previous one (Spec 1), in agreement with the inference derived from the spectral ratios. This Spec 2 can be reproduced by either an MCD model ($kT_{\text{in}} \sim 1.7$ keV) or a BB ($kT_{\text{BB}} \sim 1.3$ keV), but as shown in Table 2, the former is more successful and gives a more reasonable absorption. We hence consider that the “soft component” is approximated by an MCD model with $kT_{\text{in}} \sim 1.7$ keV.

Since the above result supports the Eastern model, the four spectra must be reproduced by a linear combination (though with different weights) of the soft component expressed by a $kT_{\text{in}} \sim 1.7$ keV MCD, and the hard component identifiable with a $kT_{\text{BB}} \sim 2.5$ keV BB. Then, adding a narrow Gaussian component to represent an Fe-K line emission line at 6–7 keV, we fitted the four spectra with this composite model, denoted MCD+BB+Gau model. The results are shown in Figure 5 and Table 3; there, r_{in} is the innermost radius of the accretion disk for an assumed inclination angle $i = 0^{\circ}$, and r_{BB} is that of the BB model assuming a spherical emission region. Thus, all the four spectra have been fitted successfully by the model, and the obtained values of $kT_{\text{in}} \sim 1.8$ keV and $kT_{\text{BB}} \sim 2.7$ keV indeed agree with those obtained by the two difference spectra. These two temperatures are also consistent

with those found in previous works that employed the Eastern model (Mitsuda et al. 1984; Makishima et al. 1989).

Can we explain these results with alternative modeling? For example, a model proposed by White et al. (1988), often called “Western” model, assumed that Thomson opacity dominates free-free opacity in the accretion disk and the emission is significantly modified by electron scattering, while the emission from the NS surface are hardly modified and observed as a simple BB emission. Then, an unsaturated Comptonized emission is expected to dominate all over the energy band, while a soft BB model is added in the intermediate range. This model can actually explain the shape of Spec 2 in terms of variations of the soft BB component. However, Spec 1 is very difficult to explain with this model, because its shape is different from those of either component of the model; we would need extreme fine tunings among the parameters of the BB and Comptonized components.

Returning to the Eastern model, a simple simulation was performed to examine the increased absorption issue in Figure 3. Employing the best fit model to Spec A, we created a fake spectrum to be called Spec A’. Yet another spectrum, named Spec B’, was created, in which the BB normalization was reduced to 67% of that of Spec A’, and the MCD normalization was set 5% higher than that in Spec A’. These are meant to emulate Spec B, within the allowed fit errors in Table Table 2. Then, the difference between Spec A’ and Spec B’ was indeed fitted successfully by a single BB model with nearly the same BB temperature as assumed in the input, but with the absorption increased to $\sim 3 \times 10^{23} \text{ cm}^{-2}$.

3.2. Absolute Values of the Physical Parameters

The Eastern model allows us to assign clear physical meanings to absolute values of the physical parameters obtained by the MCD and BB components. For that purpose, however, we need to convert the measured color temperature kT_X ($X = \text{“in”}$ or “BB”) to the effective temperature kT_X^{eff} , using so-called hardening factor κ as

$$kT_X^{\text{eff}} = \kappa^{-1} kT_X . \quad (1)$$

Then, the true radius r_X^{eff} is estimated from the measured value r_X as

$$r_X^{\text{eff}} = \kappa^2 r_X . \quad (2)$$

The value of κ is numerically estimated as 1.4–1.6 for Type I bursts (Ebisuzaki et al. 1984), and 1.7–2.0 for accretion disks (Shimura & Takahara 1995).

If we adopt $\kappa = 1.7$, the observed soft-component parameters of $kT_{\text{in}} \sim 1.8 \text{ keV}$ and $r_{\text{in}} \sim 4 \text{ km}$ yields $kT_{\text{in}}^{\text{eff}} \sim 1.1 \text{ keV}$ and $r_{\text{in}}^{\text{eff}} \sim 12 \text{ km}$. Thus, the estimated true radius

becomes larger than the NS radius of 10 km. Moreover, the value of $r_{\text{in}}^{\text{eff}}$ is close to the radius of last stable orbit in terms of general relativity, $3R_s = 12.4$ km, where $R_s \equiv 2GM/c^2$ is the Schwarzschild radius, G is the gravitational constant, M is the NS mass, and c is the light speed. As to the BB component, $kT_{\text{BB}} \sim 2.7$ keV and $r_{\text{BB}} \sim 1.2$ km yields $kT_{\text{BB}}^{\text{eff}} \sim 1.8$ keV and $r_{\text{BB}}^{\text{eff}} \sim 2.7$ km, assuming $\kappa \sim 1.5$ (London et al. 1986; Ebisuzaki 1987). The estimated $kT_{\text{BB}}^{\text{eff}}$ is close to the local Eddington temperature (2.0 keV) of a $1.4 M_\odot$ NS, suggesting that the BB emission arises from a region on the NS surface. In addition, $r_{\text{BB}}^{\text{eff}}$ is smaller than 10 km, when assuming isotropic emission from a spherical source. Therefore, as previously suggested by Mitsuda et al. (1984), the BB component can be regarded as being emitted from an equatorial zone of the NS, where the accretion disk contacts the surface.

3.3. Relations among the Model Parameters

From the above spectral analysis, it has been confirmed that the Eastern (MCD+BB+Gau) model successfully reproduces the selected four spectra in the upper-banana state, and yields physically reasonable interpretations. Given these, we applied the MCD+BB+Gau model to the 95 spectra in the upper-banana state, and obtained $\chi^2/\text{d.o.f.}$ of < 1.4 for all of them. Therefore, we regard the Eastern model as applicable to all the present data sets.

Figure 6 summarizes the relation among the unabsorbed disk bolometric luminosity L_{disk} , the unabsorbed BB bolometric luminosity for isotropic emission L_{BB} , and their sum $L_{\text{tot}} \equiv L_{\text{disk}} + L_{\text{BB}}$, as well as the temperatures and radii. Here, L_{disk} is calculated assuming a face-on disk (i.e., the inclination angle $i = 0^\circ$) as

$$L_{\text{disk}} = 2 \times \int_{r_{\text{in}}}^{\infty} 2\pi r \sigma T(r)^4 dr = 4\pi r_{\text{in}}^2 \sigma T_{\text{in}}^4, \quad (3)$$

where the first factor of 2 means emission from the two sides of the disk, σ is the Stefan-Boltzmann constant, and $T(r)$ is the disk temperature at the radius r .

In Figures 6 (a), both L_{disk} and L_{BB} are seen to increase as L_{tot} increases from 1×10^{37} to 4×10^{37} erg s $^{-1}$. However, a closer inspection reveals that L_{disk} varies more steeply than L_{BB} . Actually, the data behavior in Figure 6 (a) can be approximated as

$$L_{\text{disk}} \propto L_{\text{tot}}^{1.1}, \quad L_{\text{BB}} \propto L_{\text{tot}}^{0.7}, \quad L_{\text{BB}} \propto L_{\text{disk}}^{0.6}. \quad (4)$$

As a result, the ratio between L_{BB} and L_{disk} decreases from 0.6 to 0.4 as L_{tot} increases by a factor of 4, in agreement with previous reports (Gilfanov et al. 2003; Revnivtsev & Gilfanov 2006). Similarly, Figure 6 (b) shows the luminosity dependences of the temperature and

radius parameters, derived in the same way as in § 3.1, and presented without applying any of the correction factors mentioned in § 3.2. The relations are approximated as

$$kT_{\text{in}} \propto L_{\text{tot}}^{0.19}, \quad r_{\text{in}} \propto L_{\text{tot}}^{0.12}, \quad kT_{\text{BB}} \propto L_{\text{tot}}^{0.10}, \quad r_{\text{BB}} \propto L_{\text{tot}}^{0.11}. \quad (5)$$

Instead of L_{tot} , we may utilize the mass accretion rate \dot{M} , which can be estimated in the following way. Generally, the accreting matter releases energy at a rate of $GM\dot{M}/r_{\text{in}}$, as it flows through the disk down to the innermost radius r_{in} . According to the picture of the standard accretion disk, a half of this luminosity is radiated away in the accretion disk as $L_{\text{disk}} = \frac{1}{2} \frac{GM\dot{M}}{r_{\text{in}}}$, and the other half is stored in the Keplerian kinetic energy. Therefore, the mass accretion rate is estimated as

$$\dot{M} = \frac{2L_{\text{disk}}r_{\text{in}}}{GM} \propto L_{\text{disk}}r_{\text{in}} \propto r_{\text{in}}^3 T_{\text{in}}^4. \quad (6)$$

This relation remains valid even if r_{in} varies, as long as the disk stays in the standard state. Figure 7 shows the same physical parameters as presented in Figure 6, but this time, as a function of \dot{M} estimated via equation (6), where the unit of \dot{M} is arbitrary.

In the case of a standard accretion disk, L_{disk} and kT_{in} are expected to be proportion to \dot{M} and $\dot{M}^{0.25}$, respectively (e.g., Makishima et al. 1986; Ebisawa et al. 1993; Tanaka & Shibazaki 1996), as long as r_{in} kept constant. Indeed, in the range of $\dot{M} \lesssim 300$ (corresponding to $L_{\text{tot}} \lesssim 1.5 \times 10^{37} \text{ erg s}^{-1}$), Figure 7 reveals tight scalings as

$$L_{\text{disk}} \propto \dot{M}^{0.92 \pm 0.07}, \quad kT_{\text{in}} \propto \dot{M}^{0.21 \pm 0.05}, \quad r_{\text{in}} \propto \dot{M}^{0.05 \pm 0.07}, \quad (7)$$

which agree, within errors, with the predictions for standard disks. This result is consistent with that reported by Lin et al. (2007).

As the accretion rate \dot{M} increases to $\gtrsim 300$ in Figure 7, the disk parameters start deviating from the scalings of equation (7), and follow new relations approximated as

$$L_{\text{disk}} \propto \dot{M}^{0.80 \pm 0.03}, \quad kT_{\text{in}} \propto \dot{M}^{0.11 \pm 0.02}, \quad r_{\text{in}} \propto \dot{M}^{0.18 \pm 0.03}. \quad (8)$$

Thus, the inner disk radius r_{in} apparently starts “retreating”, with increasing fluctuations, but the increase in r_{in} is compensated by the flattering in kT_{in} . As a result, L_{disk} starts to weakly saturate, instead of increasing in proportion to \dot{M} .

Turning to the BB parameters, we find kT_{BB} rather stable, with a weak positive dependence on \dot{M} . On the contrary, r_{BB} exhibits a large scatter, which causes similar scatter in L_{BB} . The \dot{M} -dependence of these BB parameters can be approximated as

$$L_{\text{BB}} \propto \dot{M}^{0.5}, \quad kT_{\text{BB}} \propto \dot{M}^{0.07 \pm 0.01}, \quad r_{\text{BB}} \propto \dot{M}^{0.13}. \quad (9)$$

This BB behavior is the same as previously reported (Mitsuda et al. 1984; Gilfanov et al. 2003; Revnivtsev & Gilfanov 2006). We also find that kT_{BB} is always higher than kT_{in} , and r_{BB} is smaller than r_{in} . These relations are consistent with the basic assumptions of the Eastern model; the BB emission comes from the NS surface, while the MCD component from the surrounding accretion disk.

3.4. Effective Degrees of Freedom Causing Spectral Variability

We have so far described the energy spectra and their variations in terms of the four quantities, kT_{in} , r_{in} , kT_{BB} , and r_{BB} . However, it is not yet clear how many of them can be regarded as independent variables (with the rest depending on them). In other words, we need to know how many degrees of freedom are involved in the observed spectral variations in the upper-banana state. This can be done by applying “fractal dimension analysis” (e.g., Matsumoto et al. 2005) to the four model parameters.

For this purpose, let us define a 4-dimensional vector space spanned by the four variables, $Y_1 = kT_{\text{in}}$, $Y_2 = r_{\text{in}}$, $Y_3 = kT_{\text{BB}}$, and $Y_4 = r_{\text{BB}}$, wherein each data set is represented by a vector

$$V(\vec{i}) = \{Y_1(i), Y_2(i), Y_3(i), Y_4(i)\}$$

with $i = 1, 2, \dots, 95$ denoting the data number. Let us also define the average vector $\langle \vec{V} \rangle = \Sigma_{i=1}^{95} V(\vec{i})/95 \equiv \{\langle Y_1 \rangle, \langle Y_2 \rangle, \langle Y_3 \rangle, \langle Y_4 \rangle\}$, and the zero-mean vectors, $v(\vec{i}) = V(\vec{i}) - \langle \vec{V} \rangle \equiv \{y_1(i), y_2(i), y_3(i), y_4(i)\}$ with $y_k(i) \equiv Y_k(i) - \langle Y_k \rangle$. Then, a “distance” $D(i)$ of the vector $v(\vec{i})$, measured from the origin, is calculated as

$$D(i) = \left[\sum_{k=1}^4 \{y_k(i)/\sigma_k\}^2 \right]^{1/2} \quad (i = 1, 2, \dots, 95), \quad (10)$$

where $\sigma_k = [\Sigma_{i=1}^{95} y_k(i)^2/94]^{1/2}$ is the standard deviation in $y_k(i)$ around the origin [or in $Y_k(i)$ around its mean $\langle Y_k \rangle$]. Finally, we calculate the number $N(< D)$ of those data points of which the distance $D(i)$ is less than a given value D .

Figure 8 shows the normalized data point number $N(< D)/95$ from equation (10) as a function of D , over the range of $N/95 = 0.2 - 0.8$ (or $N = 23 - 76$). If the variations are controlled by n ($1 \leq n \leq 4$) independent parameters, we expect the vectors $v(\vec{1}), v(\vec{1}), \dots, v(\vec{95})$ to form a n -dimensional subspace in the vector space, so that $N(< D)$ should increase as $\propto D^n$. Indeed, Figure 8 reveals a tight power-law relation as

$$N \propto D^{1.8 \pm 0.1}. \quad (11)$$

Since this result is consistent with $n = 2$, we infer that the spectral behavior in the upper-banana state of 4U 1608–522 has effectively two degrees of freedom.

3.5. Fluctuations Independent of the Total Luminosity

Of the two independent variables describing the spectral variability (§ 3.4), one is obviously the total luminosity L_{tot} , or nearly equivalently, the mass accretion rate \dot{M} . Actually in Figure 6 (or Figure 7), the four quantities are all observed to depend primarily on L_{tot} (or \dot{M}). However, they show significant scatters around the L_{tot} -dependent correlation, so that none of them can be regarded as a single-valued function of L_{tot} (or \dot{M}). This is consistent with the presence of the second degree of freedom revealed in § 3.4. In order to identify what is causing this extra freedom, we remove the L_{tot} -dependence from the behavior of the four model parameters, and study the residual variations.

To eliminate the major L_{tot} -dependence from the physical parameters, we calculated their de-trended counterparts $Z'(i)$ ($Z = L_{\text{disk}}, L_{\text{BB}}, kT_{\text{in}}, r_{\text{in}}, kT_{\text{BB}}$ and r_{BB}), employing equations (4) and (5), as

$$L'_{\text{disk}}(i) \propto L_{\text{disk}}(i)/L_{\text{tot}}(i)^{1.1}, \quad L'_{\text{BB}}(i) \propto L_{\text{BB}}(i)/L_{\text{tot}}(i)^{0.7}, \quad (12)$$

$$kT'_{\text{in}}(i) \propto kT_{\text{in}}(i)/L_{\text{tot}}(i)^{0.19}, \quad r'_{\text{in}}(i) \propto r_{\text{in}}(i)/L_{\text{tot}}(i)^{0.12}, \quad (13)$$

$$kT'_{\text{BB}}(i) \propto kT_{\text{BB}}(i)/L_{\text{tot}}(i)^{0.10}, \quad \text{and} \quad r'_{\text{BB}}(i) \propto r_{\text{BB}}(i)/L_{\text{tot}}(i)^{0.11}. \quad (14)$$

(As the de-trending parameter, we chose L_{tot} rather than \dot{M} , because the latter is less directly estimated from the data.) Absolute values of the de-trended parameters are not meaningful, and we hereafter consider their relative values only. Since r'_{in} shows the largest variation among them, we plot in Figure 9 the de-trended parameters as a function of r'_{in} . Table 4 also summarizes those of Spec A to D in § 3.1. From the behavior of the de-trended luminosities, the data points can be divided into two branches; one has almost constant luminosities as r'_{in} varies, while the other is characterized by significant r'_{in} -dependent variations both in L'_{disk} and L'_{BB} . Hereafter, the two branches are denoted as “constant-luminosity branch (CLB)” and “variable-luminosity branch (VLB)”, respectively. The two branches may connect at $r'_{\text{in}} \sim 0.85$, rather than behaving independently from each other.

In the CLB, the de-trended BB luminosity stays nearly constant at $L'_{\text{BB}} \sim 0.8$; so are the two BB parameters, $kT'_{\text{BB}} \sim 1.6$ and $r'_{\text{BB}} \sim 0.9$. Similarly, the de-trended disk luminosity remains at $L'_{\text{disk}} \sim 0.9$. As a result, the CLB data points are distributed in Figure 6 (a) along the major correlation trends. Nevertheless, r'_{in} varies by $\sim \pm 20\%$, accompanied by a clear decrease in the de-trended disk temperature as $kT'_{\text{in}} \propto r_{\text{in}}^{-0.5}$. (This scaling is a natural consequence of the constant L'_{disk} and the relation of $L'_{\text{disk}} \propto r_{\text{in}}^2 T_{\text{in}}'^4$.) There are two

possibilities to explain this r'_{in} behavior. One is real changes in r_{in} , and the other is those in the color hardening factor κ of the disk. Since L'_{disk} is kept constant in the CLB, the latter case may be more likely. Specifically, the observed behavior will be explained if some unspecified mechanisms (possibly related to vertical structure changes in the disk) caused κ to increased by $\sim 10\%$ while somehow keeping the effective temperature of the disk and its true radius constant; the observed color temperature kT'_{in} would then increase by $\sim 10\%$ according to equation (1), and the apparent disk radius r'_{in} would decrease by $\sim 20\%$ after equation (2), thus reproducing the observaton.

In the VLB, r'_{in} varies over a relatively small range ($\sim \pm 10\%$), whereas the two luminosities both vary significantly in an anti-correlated way; L'_{disk} decreases from 1.9 to 1.5 as $\propto r'_{\text{in}}^{-1}$, while L'_{BB} increases from 0.8 to 1.2 as $\propto r'_{\text{in}}^2$. This complementary behavior between the MCD and BB components appears in Figure 6 as the large fluctuations away from the major trend, where the data points reach a level of $L_{\text{disk}} \sim L_{\text{BB}} \sim 0.5L_{\text{tot}}$. (This behavior cannot be a fitting artifact caused by strong couplings between the two spectral component, since the nominal fitting errors are not particularly larger in the VLB, and are generally smaller than/comparable to the size of the plotting symbols in Figure 6 and Figure 7.) Since kT'_{BB} is almost constant (or only slightly decreasing) like in the CLB, the increase of L'_{BB} is mainly caused by that of r'_{BB} from 0.9 to 1.2 as $\propto r'_{\text{in}}^1$. We again observe kT'_{in} to decrease like in the CLB, but with a different r'_{in} -dependence which is approximated as $\propto r'_{\text{in}}^{-0.75}$. This is exactly the behavior of a standard accretion disk (Shakura & Sunyaev 1973) when its radius varies under a constant \dot{M} , because we then expect $\dot{M} \propto r_{\text{in}}^3 T_{\text{in}}^4$ (equation (6)). This also explains the observed disk luminosity behavior, as $L'_{\text{disk}} \propto r_{\text{in}}^2 T_{\text{in}}^4 \propto r'_{\text{in}}^{-1}$. Obviously, the increase in the disk radius under a constant \dot{M} predicts that a larger fraction of the overall gravitational energy release should be emitted by the BB component; in fact, along the full VLB in Figure 7(b), L'_{disk} is seen to decrease by ~ 0.3 in the employed arbitrary unit, while L'_{BB} to increase by ~ 0.3 , thus conserving the total luminosity. In other words, the VLB is characterized by actual changes in the innermost disk radius.

Based on these correlation analyses among the de-trended spectral parameters, we conclude that the second independent variable (besides \dot{M} ; § 3.4) causing the variability in the upper-banana state can be ascribed to sporadic changes in r'_{in} (or in r_{in}). However, this r'_{in} variability is likely to be further subdivided into two different mechanisms under a constant \dot{M} ; one is an apparent effect due to variations in κ of the disk, and the other is real changes.

As shown in Figure 9 and Table 4, the L'_{disk} parameters of Spec B, C and D locate on the CLB line, while that of Spec A does on the VLB one. Therefore, we consider that the hard/soft-band differences of Spec A/B and C/D observed in Figure 2 are mainly attributed to the VLB and CLB variation, respectively. On the other hand, the de-trended parameters

of Spec B and C are similar, and the variability between them observed over the entire 3–30 keV band is thought to be dominated by the \dot{M} change.

4. DISCUSSION AND CONCLUSION

4.1. The Eastern Model

Through the analysis of the *RXTE* spectra of the atoll source 4U 1608–522 in its upper-banana state, we have confirmed that both time-averaged and difference energy spectra can be reproduced successfully by the Eastern (MCD+BB+Gau) model. Considering the hardening factor, the effective temperature and radius of the MCD component were obtained as $kT_{\text{in}}^{\text{eff}} \sim 1.1$ keV and $r_{\text{in}}^{\text{eff}} \sim 12$ km, respectively. The radius is larger than the representative NS radius, 10 km, and is consistent with the last stable orbit, $3R_s = 12.4$ km, allowed by general relativity. This result agrees with the picture of a standard accretion disk which is formed around a NS. The BB parameters were found as $kT_{\text{BB}}^{\text{eff}} \sim 1.8$ keV and $r_{\text{BB}}^{\text{eff}} \sim 2.7$ km, assuming isotropic emission from a spherical source. The temperature is close to the local Eddington temperature (2.0 keV) at the NS surface, and the radius is smaller than 10 km. Then, the BB component can be regarded as being emitted from an equatorial zone of the NS, as previously suggested by Mitsuda et al. (1984).

4.2. Saturation of the Blackbody Luminosity

According to the picture of standard accretion disks, a half of the released gravitational energy is radiated from the accretion disk (L_{disk}), and the other half is stored in the Keplerian kinetic energy and then emitted (L_{BB}) when the matter settles onto the NS surface. Then, we expect L_{BB} to be proportion to L_{disk} , and hence the $L_{\text{BB}}/L_{\text{disk}}$ ratio to be constant. Indeed, L_{disk} was found to increase almost linearly with the total luminosity L_{tot} (figure 6a). However, the same figure reveals that L_{BB} increases less steeply, making the $L_{\text{BB}}/L_{\text{disk}}$ ratio decrease from 0.6 to 0.4 as L_{tot} increases from 1×10^{37} to 4×10^{37} erg s $^{-1}$.

We may think of two possibilities to explain the observed relative decrease of L_{BB} . One is that the accreting matter reaches the NS surface and emits L_{BB} which is equivalent to the Keplerian energy (i.e. $\propto L_{\text{disk}}$), but we cannot observe all the emission because its wavelength shifts outside the PCA energy band (3–30 keV), or the geometrical angle of the emission moves from our line of sight. However, we have not observed any hint of extra emission in the softest or hardest energy ends of the PCA spectra. In addition, other sources, which are thought to have different inclination angles, are also reported to show the same behavior of

the decreasing $L_{\text{BB}}/L_{\text{disk}}$ ratio (Revnivtsev & Gilfanov 2006). Therefore, this possibility is unlikely.

The other possibility is that the accreting matter flows all the way through the disk down to its inner radius that is close to the NS surface, but its progressively larger fraction fails to accrete onto the NS surface. If the accretion-failed matter stayed around the NS away from the surface (e.g., an expansion of the boundary layer), it would accumulate to become optically thick, eventually producing detectable emission. This would lead to a decrease in kT_{BB} , because the emission radius should increase. As shown in Figure 6 and equation (5), however, this is not the case; the kT_{BB} value stays almost constant (or rather increases) as the total luminosity increases. Then, a fraction of the matter must be outflowing and escaping from the system without releasing its kinetic energy as emission. Although the observed $L_{\text{tot}} \sim 4 \times 10^{37} \text{ erg s}^{-1}$ is only $\sim 20\%$ of the Eddington luminosity for a $1.4 M_{\odot}$ NS, the observed value of $kT_{\text{BB}}^{\text{eff}} \sim 1.8 \text{ keV}$ is already close to the spherical Eddington temperature at 10 km (2.0 keV). Considering further the non-spherical geometry of the disk, and the disk radius which is possibly larger than 10 km, the putative outflow is likely to be driven by increased radiation pressure in the innermost disk region. The presence of such outflows is indeed suggested by detections of broad absorption features from LMXBs (Schulz & Brandt 2002; Ueda et al. 2004), black hole binaries (Kotani et al. 2000; Yamaoka et al. 2001; Kubota et al. 2007), and active galactic nuclei (Pounds et al. 2003ab).

Assuming that the decrease in $L_{\text{BB}}/L_{\text{disk}}$ from 0.6 to 0.4 is due to outflows, about $(0.6 - 0.4)/0.6 \sim 30\%$ of the accreting matter is estimated to escape from the system at a typical luminosity of $\sim 4 \times 10^{37} \text{ erg s}^{-1}$. Toward lower luminosities, the ratio appears to converge to ~ 0.6 , rather than 1.0 which would be theoretically expected. This may be attributed to effects due, e.g., to the system inclination, general relativity, and NS rotation (e.g., Sunyaev & Shakura (1986)). Detailed theoretical discussion on this point is beyond the scope of the present paper.

As indicated by equation (8), the innermost disk radius r_{in} is observed to increase gradually when the mass accretion rate increases to $\gtrsim 300$ in Figure 7, or equivalently, when the total luminosity becomes $\gtrsim 1.5 \times 10^{37} \text{ erg s}^{-1}$ (corresponding to $\gtrsim 7\%$ of the Eddington luminosity). This is unlikely to be an apparent effect caused, e.g., by changes in the hardening factor, since this quantity would increase as the luminosity increases (Gierliński & Done 2003; Davis et al. 2005), and would hence make r_{in} smaller. Therefore, the increase in r_{in} toward higher accretion rates is considered to represent a real retreat of the innermost disk radius. This interpretation may agree with the results by Popham & Sunyaev (2001), who numerically calculated the physical condition of the boundary layer and showed that the disk inner edge retreats back by the increased radiation pressure when the luminosity approaches

the Eddington limit.

4.3. Secondary Spectral Variations

The result of the fractal dimension analysis shows that the source variations are controlled by two independent variables. One of them is obviously the mass accretion rate (or nearly equivalently the total luminosity), which produces the major trend in Figure 7 as discussed so far. The other variable is thought to be random changes in the inner disk radius, as represented by the behavior of r'_{in} in the de-trended analysis performed in § 3.5. As discussed therein, the variations of r'_{in} may be caused by two different mechanisms, corresponding to the CLB and VLB. These two branches are considered to degenerate in the fractal dimension analysis, and difficult to identify as two independent degrees of freedom.

In the CLB, the change in r'_{in} seems to be apparent rather than real, and is considered to reflect fluctuations in the hardening factor of the disk. As a result, the BB parameters remain unchanged, while the MCD parameters vary as $kT'_{\text{in}} \propto r'_{\text{in}}{}^{-0.5}$, keeping the disk luminosity constant ($L'_{\text{disk}} \propto r'_{\text{in}}{}^0$). Such variations in the hardening factor may in turn stem, e.g., from fluctuations of the disk height, because this would affect the temperature gradient and/or radiative transfer in the vertical direction of the disk.

In the VLB, the change in r'_{in} is considered real (§ 3.5), because we observe a scaling of $kT'_{\text{in}} \propto r'_{\text{in}}{}^{-0.75}$ which agrees with the behavior of a standard accretion disk under a constant \dot{M} and a constant hardening factor. In this branch, the disk is considered to randomly retreat back from its “home position”, which is located in Figure 9 around $r'_{\text{in}} \sim 0.85$ where the CLB and VLB meet. When this takes place, the accreting matter located between the retreated and the home-position radii will fall onto the NS surface without radiating the disk emission, and the gravitational energy it acquires will be released solely as the radiation from the NS surface. Then, L_{disk} will decrease while L_{BB} will increase. This can naturally explain the anti correlation between the MCD and BB luminosities observed in the VLB (Figure 9).

4.4. Conclusion

The results of our study can be summarized in the following four points.

1. The physical picture provided by the Eastern model can consistently explain the behavior of 4U 1608–522 in the upper-banana state.

2. When the mass accretion rate increases, some fraction of the matter flowing through the accretion disk starts outflowing, presumably due to an increased radiation pressure.
3. Even at the same accretion rate, the spectral parameter changes randomly on time scales of hours to days, mainly reflecting changes in the innermost disk radius.
4. The change in the disk inner radius is a mixture of real and apparent effects, the former due to sporadic retreat of the disk while the latter due to fluctuations in the color hardening factor.

Facilities: RXTE (PCA).

REFERENCES

- Bradt, H. V., Rothschild, R. E., & Swank, J. H. 1993, A&AS, 97, 355
- Church, M. J., & Balucińska-Church, M. 2004, MNRAS, 348, 955
- Davis, S. W., Blaes, O. M., Hubeny, I., & Turner, N. J. 2005, ApJ, 621, 372
- Ebisawa, K., Makino, F., Mitsuda, K., Belloni, T., Cowley, A. P., Schmidtke, P. C., & Treves, A. 1993, ApJ, 403, 684
- Ebisuzaki, T., Sugimoto, D., & Hanawa, T. 1984, PASJ, 36, 551
- Ebisuzaki, T., PASJ, 39, 287
- Gierliński, M. & Done, C. 2002a, MNRAS, 331, L47
- Gierliński, M. & Done, C. 2002b, MNRAS, 337, 1373
- Gierliński, M. & Done, C. 2003, MNRAS, 347, 885
- Gilfanov, M., Revnivtsev, M. & Molkov, S. 2003, A&A, 410, 217
- Grindlay, J. E., & Liller, W. 1978, ApJ, 220, L127
- Hasinger, G., & van der Klis, M. 1989, A&A, 225, 79
- Inogamov, N. A., & Sunyaev, R. A. 1999, Astro. Lett., 25, 269
- Jahoda, K., Markwardt, C. B., Radeva, Y., Rots, A. H., Stark, M. J., Swank, J. H., Strohmayer, T. E., & Zhang, W. 2006, ApJS, 163 401

- Jahoda, K., Swank, J. H., Giles, A. B., Stark, M. J., Strohmayer, T., Zhang, W., & Morgan, E. H. 1996 *Proc. SPIE*, 2808, 59
- Kotani, T., Ebisawa, K., Dotani, T., Inoue, H., Nagase, F., Tanaka, Y., & Ueda, Y. 2000, *ApJ*, 539, 413
- Kubota, A., Tanaka, Y., Makishima, K., Ueda, Y., Dotani, T., Inoue, H., & Yamaoka, K. 1998, *PASJ*, 50, 667
- Kubota, A. et al. 2007, *PASJ*, 59S, 185
- Lin, D., Remillard, R. A., & Homan, J. 2007, *ApJ*, 667, 1073
- London, R. A., Taam, R. E., & Howard, W. M. 1986, *ApJ*, 306, L170
- Makishima, K., Ishida, M., Ohashi, T., Dotani, T., Inoue, H., Mitsuda, K., Tanaka, Y., Turner, M. J. L., & Hoshi, R. 1989, *PASJ*, 41, 531
- Makishima, K., Maejima, Y., Mitsuda, K., Bradt, H. V., Remillard, R. A., Tuohy, I. R., Hoshi, R., & Nakagawa, M. 1986, *ApJ*, 308, 635
- Matsumoto, Y., Makishima, K., Kotoku, J., Yoshimori, M., Suga, K., Kosugi, T., Masuda, S., & Morimoto, K. 2005, *PASJ*, 57, 211
- Mitsuda K., Inoue, H., Koyama, K., Makishima, K., Matsuoka, M., Ogawara, Y., Suzuki, K., Tanaka, Y., Shibasaki, N., & Hirano, T. 1984, *PASJ*, 36, 741
- Mitsuda, K., Inoue, H., Nakamura, N., & Tanaka, Y. 1989, *PASJ*, 41, 97
- Muno, M. P., Remillard, R. A., & Chakrabarty, D. 2002, *ApJ*, 568, L35
- Nakamura, N., Dotani, T., Inoue, H., Mitsuda, K., Tanaka, Y., & Matsuoka, M. 1989, *PASJ*, 41, 617
- Popham, R., & Sunyaev, R. 2001, *ApJ*, 547, 355
- Pounds, K. A., Reeves, J. N., King, A. R., Page, K. L., O’Brien, P. T., & Turner, M. J. L. 2003, *MNRAS*, 345, 705
- Pounds, K. A., King, A. R., Page, K. L., & O’Brien, P. T. 2003, *MNRAS*, 346, 1025
- Revnivtsev, M. & Gilfanov, M. 2006, *A&A*, 453, 253
- Rutledge, R. E., Bildsten, L., Brown, E. F., Pavlov, G. G., & Zavlin, V. E. 1999, *ApJ*, 514, 945

- Shakura, N. I., & Sunyaev, R. A. 1973, A&A, 24, 337
- Shimura, T., & Takahara, F. 1995, ApJ, 445, 780
- Schulz, N. S., & Brandt, W. N. 2002 ApJ, 572, 971
- Sunyaev, R. A., & Shakura, N. I. 1986, Soviet Ast., 12, 117
- Tanaka, Y., & Shibazaki, N. 1996, ARA&A, 34, 607
- Ueda, Y., Murakami, H., Yamaoka, K., Dotani, T., & Ebisawa, K. 2004, ApJ, 609, 325
- White, N. E., Stella, L., & Parmar, A. N. 1988, ApJ, 324, 363
- Yamaoka, K., Ueda, Y., Inoue, H., Nagase, F., Ebisawa, K., Kotani, T., Tanaka, Y., & Zhang, S., N. 2001, PASJ, 53, 179
- Zimmerman, E. R., Narayan, R., McClintock, J. E., & Miller, J. M. 2005, ApJ, 618, 832

Table 1: Four spectra analyzed circumstantially in the upper-banana state.

Spectrum	Observation	Count Rate [Crab]	Color	
	ID		Soft ^a	Hard ^b
Spec A	30062-03-01-02	1.07	0.43	0.29
Spec B	30062-03-01-01	1.03	0.41	0.26
Spec C	30062-03-01-00	0.95	0.40	0.25
Spec D	30062-03-01-04	0.78	0.42	0.27

^a The soft color refers to the source count ratio of 6–10 keV / 2.5–6 keV.

^b The same as the soft color but the ratio of 10–30 keV / 6–10 keV counts.

Table 2: Model fit results to the difference spectra calculated from those in Table 1.^a

Spectrum	Model	N_{H} ^b	kT_{BB} ^c	kT_{in} ^c	$\chi^2/\text{d.o.f.}$
Spec 1 (A - B)	BB	27^{+12}_{-11}	2.5 ± 0.1	\dots	20/58
Spec 2 (C - D)	BB	< 0.3	1.27 ± 0.02	\dots	47/58
	MCD	1.8 ± 1.2	\dots	1.7 ± 0.1	29/58

^a All the errors are single-parameter 90% confidence limits.

^b The absorption column density in the unit of 10^{22} cm^{-2} .

^c Temperatures are all in the unit of keV.

Table 3: Fitting results of the four original spectra in Table 1 with the MCD+BB+Gau model.^a

Spectrum	MCD		BB		Gau ^b		$\chi^2/\text{d.o.f.}$
	kT_{in} ^c	r_{in} ^d	kT_{BB} ^c	r_{BB} ^e	Cen. Ene. ^f	Norm ^g	
Spec A	$1.84^{+0.03}_{-0.04}$	$4.1^{+0.1}_{-0.2}$	2.67 ± 0.04	1.5 ± 0.1	6.6 ± 0.2	$1.9^{+0.5}_{-0.4}$	29/54
Spec B	1.88 ± 0.04	$4.0^{+0.1}_{-0.2}$	$2.78^{+0.1}_{-0.08}$	1.1 ± 0.1	6.6 ± 0.2	2.0 ± 0.4	41/54
Spec C	1.79 ± 0.04	$4.2^{+0.2}_{-0.1}$	2.64 ± 0.08	1.2 ± 0.1	$6.6^{+0.2}_{-0.1}$	1.7 ± 0.4	32/54
Spec D	1.84 ± 0.06	$3.5^{+0.3}_{-0.2}$	2.7 ± 0.1	$1.1^{+0.2}_{-0.1}$	6.6 ± 0.2	$1.1^{+0.4}_{-0.3}$	42/54

^a All the errors are single-parameter 90% confidence limits. The absorption column density is fixed at $0.8 \times 10^{22} \text{ cm}^{-2}$.

^b The width of the Gaussian component is not well determined and constraint to be $\leq 0.2 \text{ keV}$.

^c Temperatures are all in the unit of keV.

^d The innermost radius in the unit of $\sqrt{\cos i}^{-1} \text{ km}$, where i is the inclination angle.

^e The radius of the BB emission in the unit of km, assuming the emission comes from the isotropic sphere region.

^f The center energy of the Gaussian model, which is limited in the range of 6.4–6.9 keV.

^g The normalization of the Gaussian model in the unit of $10^{-2} \text{ photons cm}^{-2} \text{ s}^{-1}$.

Table 4: de-trended parameters of Spec A to D after eliminating the L_{tot} dependence in Figure 9.^{a,b}

	L'_{disk}	L'_{BB}	kT'_{in}	r'_{in}	kT'_{BB}	r'_{BB}
Spec A	1.69	1.11	1.43	0.97	1.58	1.15
Spec B	1.96	0.75	1.49	0.96	1.65	0.86
Spec C	1.93	0.80	1.44	1.04	1.58	0.97
Spec D	1.90	0.85	1.53	0.88	1.64	0.92

^a See equation (14) for the L_{tot} -dependence eliminated here.

^b Absolute values of the de-trended parameters are not meaningful.

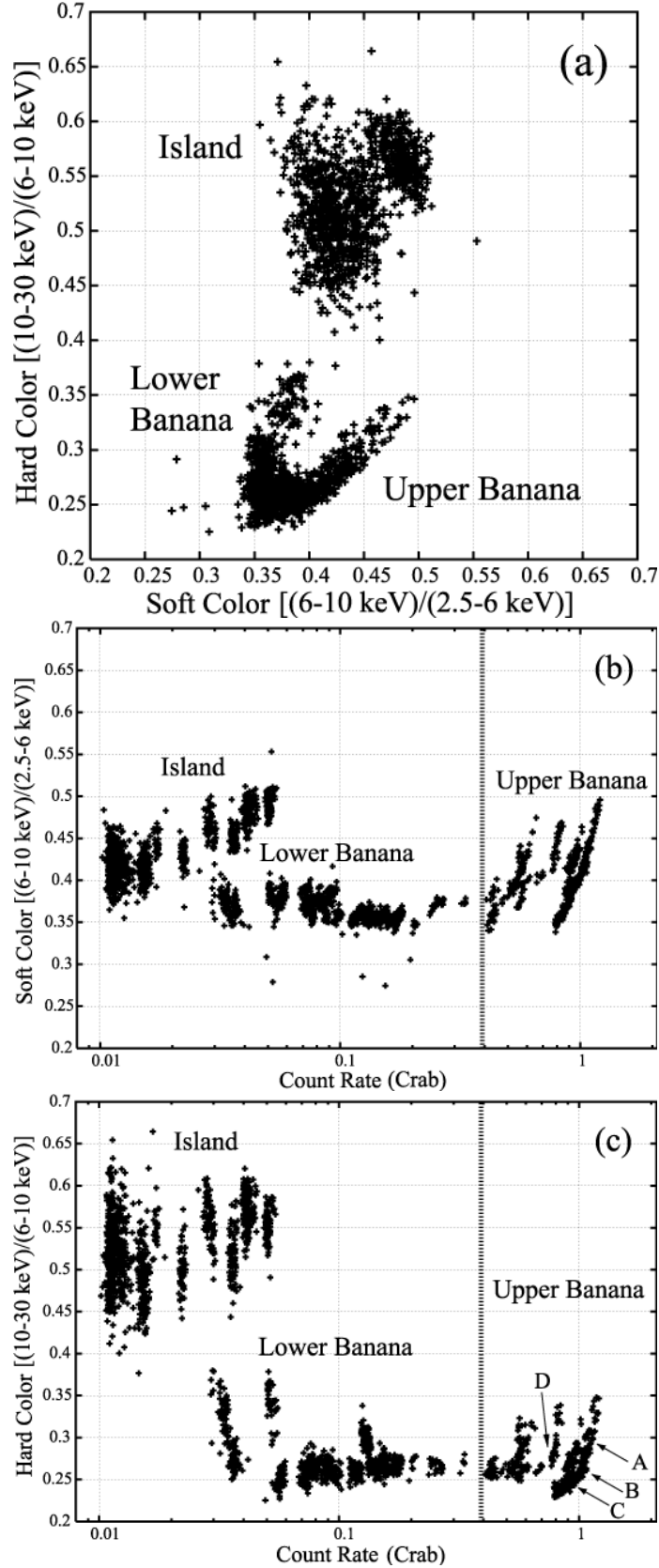


Fig. 1.— The CCD (panel a), soft-HID (panel b), and hard-HID (panel c) of 4U 1608–522 in epoch 3, with the time bin of 128 s. The utilized energy bands are described in the text. Four arrows indicate the datasets analyzed in § 3.1 (Table 1).

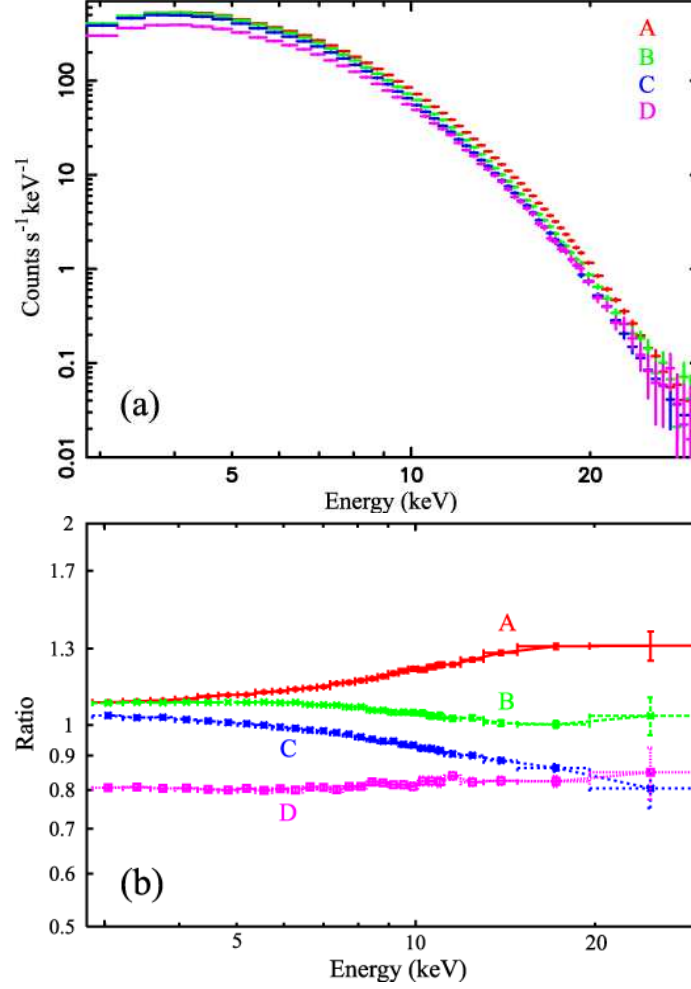


Fig. 2.— Four energy spectra (panel a) shown in Table 1 and Figure 1 (c), and their intensity ratios to their average (panel b). The energy spectra are shown without removing the detector response.

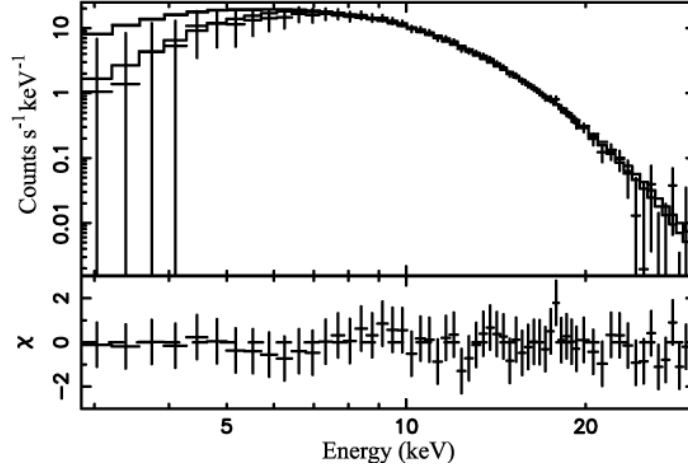


Fig. 3.— The difference spectrum (Spec 1) between the brightest (Spec A) and the second brightest (Spec B) spectra in Figure 2. It is successfully represented by an absorbed BB model with a temperature $kT_{\text{BB}} \sim 2.5$ keV (lower histogram). The fit residuals are shown in the bottom panels. If the absorption is fixed at $0.8 \times 10^{22} \text{ cm}^{-2}$, the model over-predicts the data below 7 keV (upper histogram).

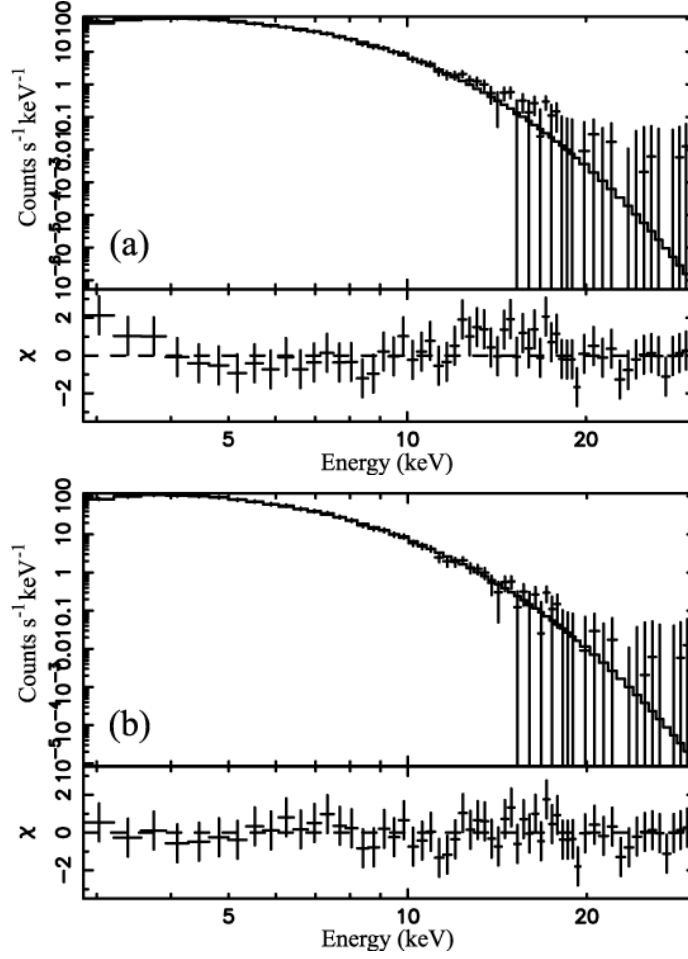


Fig. 4.— The same as Figure 3, but for the difference (Spec 2) between the faintest spectrum (Spec D) and the second faintest one (Spec C) in Figure 2. It is reproduced by either a BB model (panel a, $kT_{\text{BB}} \sim 1.3$ keV) or an MCD model (panel b, $kT_{\text{in}} \sim 1.7$ keV), with the absorption column density left free.

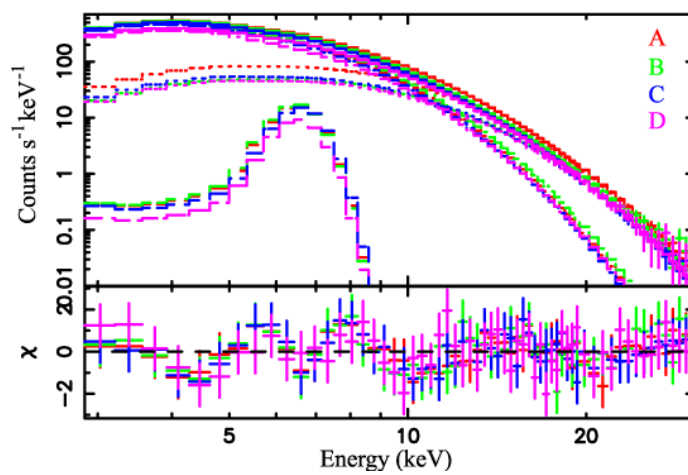


Fig. 5.— The same four spectra as presented in Figure 2 (a), fitted by an MCD+BB+Gau model with the absorption column density fixed at $0.8 \times 10^{22} \text{ cm}^{-2}$.

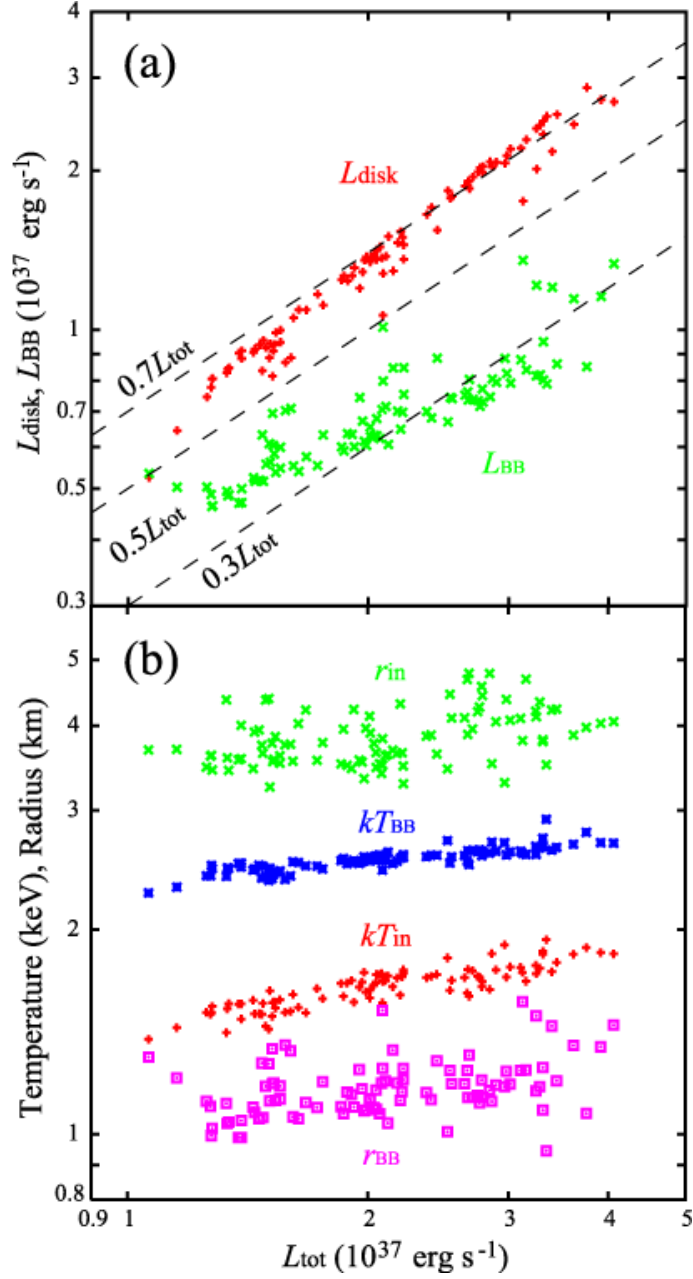


Fig. 6.— (a) The relations of the MCD luminosity (L_{disk}) and the BB luminosity (L_{BB}) as a function of $L_{\text{tot}} \equiv L_{\text{disk}} + L_{\text{BB}}$ in the upper-banana state. Each data point represents one of the 95 observations. The three dashed lines show $0.7L_{\text{tot}}$, $0.5L_{\text{tot}}$, and $0.3L_{\text{tot}}$, from top to bottom. (b) The same as (a) but for the temperatures and radii of the MCD and BB models.

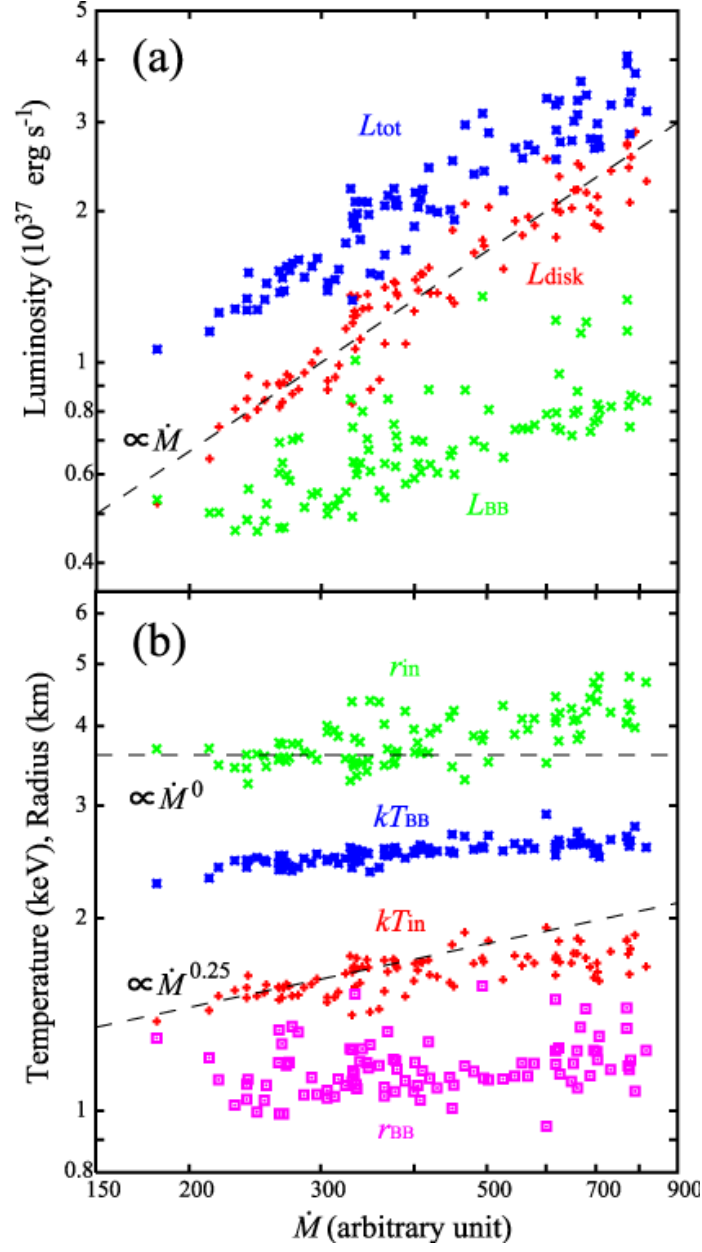


Fig. 7.— The same as Figure 6, but shown as a function of the estimated mass accretion rate \dot{M} . The three dashed lines illustrate dependences as $L_{\text{disk}} \propto \dot{M}$, $r_{\text{in}} \propto \dot{M}^0$, and $kT_{\text{in}} \propto \dot{M}^{0.25}$.

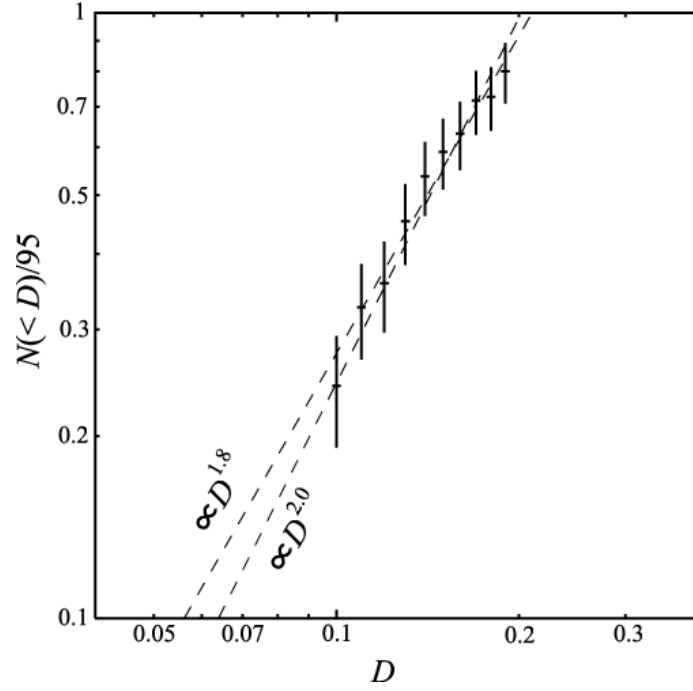


Fig. 8.— Results of the fractal dimension analysis of the four model parameters (kT_{in} , r_{in} , kT_{BB} , and r_{BB}) over the 95 data sets. See text for details.

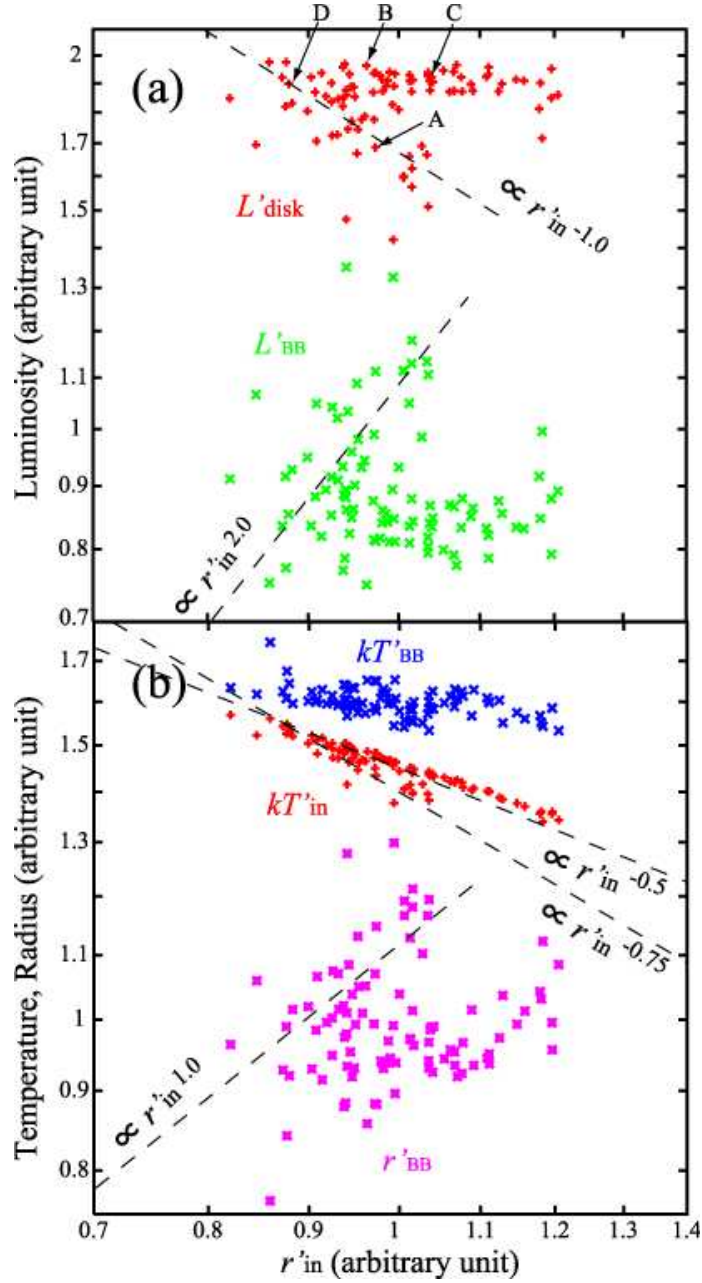


Fig. 9.— The same as Figure 6, but for the physical parameters from which the L_{tot} dependence was removed via equations (12)–(14). They are plotted as a function of the de-trended innermost radius of the accretion disk r'_{in} . Dashed lines indicate the relations of $r'_{\text{in}}{}^p$, with $p = -1.0, -0.75, -0.5, 1.0$ and 2.0 . The L'_{disk} parameters of Spec A to D in Table 4 are also indicated.